PCCP

Accepted Manuscript

ROYAL SOCIETY OF CHEMISTRY

www.rsc.org/pccp

STRUCTURAL AND DEFECT CHEMISTRY GUIDELINES FOR $Sr(V,Nb)O_3$-BASED SOFC ANODE MATERIALS

J. Macías [a], A.A. Yaremchenko* [a], D.P. Fagg [b], J.R. Frade [a]

[a] CICECO – Aveiro Institute of Materials, Department of Materials and Ceramic Engineering, University of Aveiro, 3810-193 Aveiro, Portugal

[b] TEMA-NRD, Mechanical Engineering Department, University of Aveiro, 3810-193 Aveiro, Portugal

* Corresponding author. Fax: +351-234-370204; Tel: +351-234-370235;
e-mail: ayaremchenko@ua.pt

Table of Contents Entry

Substitution with Nb into $SrVO_3$ is demonstrated to expand stability domain of cubic perovskite phase and to suppress unfavorable thermochemical expansion, while preserving sufficiently high electronic conductivity required for SOFC anode material.

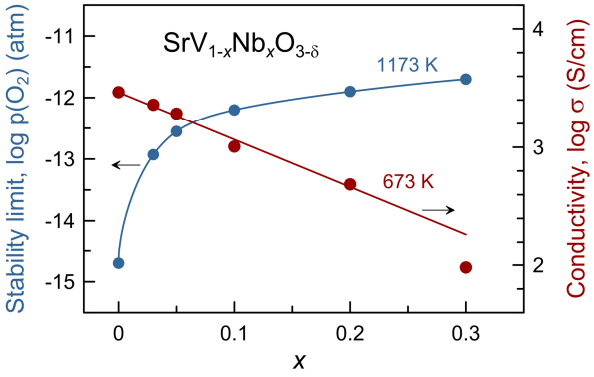

Abstract

Structural and defect chemistry guidelines were used for Nb-substituted $SrVO_{3-\delta}$ materials, designed to meet SOFC anode requirements, with emphasis on redox tolerance, thermochemical compatibility with other SOFC materials, electrical conductivity and adjustable changes in oxygen stoichiometry for their prospective impact on electrocatalytic performance. $SrV_{1-x}Nb_xO_{3-\delta}$ (x = 0-0.30) ceramics were prepared by solid-state synthesis and sintered at 1773 K in reducing atmosphere. XRD and SEM/EDS showed that under these conditions single-phase cubic perovskite structure occurs for up to $x \approx 0.25$. Electrical conductivity is metallic-like and nearly $p(O_2)$-independent. Although substitution with niobium decreases conductivity, which still exceeds 100 S/cm for $x \leq 0.20$ at temperatures below 1273 K, it also expands stability domain of cubic perovskite phase and suppresses partly high thermochemical expansion characteristic for parent $SrVO_{3-\delta}$. The upper $p(O_2)$ limit of phase stability was found to shift from ~ 2×10^{-15} atm for undoped material to ~ 2×10^{-12} atm for $x = 0.30$, whereas the average thermal expansion coefficient at 773-1223 K decreased from 22.7×10^{-6} to 13.3×10^{-6} K^{-1}. $SrV_{1-x}Nb_xO_{3-\delta}$ perovskites undergo oxidative decomposition in air, which causes dimensional and microstructural changes. However, sluggish kinetics of oxidation under inert gas conditions results in nearly reversible behavior in relatively short-term redox cycles between reducing and inert atmospheres. Subtle structural changes and close correlation with point defect chemistry clarify these sluggish changes and provide guidelines to retain metastability.

1. Introduction

Limitations of conventional solid oxide fuel cell (SOFC) anodes based on Ni-YSZ (yttria-stabilized zirconia) cermets, such as poor redox and microstructural stability and degradation due to coking and sulfur poisoning in hydrocarbon fuels [1-4], have stimulated the search for alternative electrode materials. Particular attention has been focused on ceramic components with electronic or, preferably, mixed ionic-electronic conductivity capable to replace metallic nickel in composite electrodes or to function as single-phase fuel electrodes.

The most widely studied ceramic materials for fuel electrodes are based on strontium titanate; this relies on the outstanding redox stability of $SrTiO_3$ combined with ability of oxide materials to hinder coking, and also sulphur tolerance. However, its conductivity is often below 10 S/cm under prospective operation conditions of fuel electrodes, implying significant current collection limitations. Though high conductivity can be attained after firing at high temperatures under very reducing conditions, this is probably a metastable condition, undergoing long term degradation in operating conditions. Thus, other materials are attracting increasing interest as prospective fuel materials, including strontium vanadate, $SrVO_{3-\delta}$, and its derivatives [5-15]. $SrVO_{3-\delta}$ with cubic perovskite-type structure is known to exhibit high electronic conductivity under anode operation conditions (~ 1000 S/cm at 1073 K and $p(O_2) \sim 10^{-20}$ atm) [5,6,15-18]. Although the level of oxygen-ionic conductivity in $SrVO_{3-\delta}$ has never been reported, this oxide exhibits significant oxygen deficiency (δ up to ~ 0.1 at room temperature [17-20]), and, therefore, one may consider a contribution of ionic conduction to transport properties and electrocatalytic performance. Cermet anodes made of La-substituted $SrVO_{3-\delta}$ with YSZ or doped ceria were reported to demonstrate fairly good electrochemical performance in both H_2 and wet CH_4 as fuels, without carbon deposition in the latter case [7-11]. Furthermore, $SrVO_{3-\delta}$-based anodes show a high tolerance towards H_2S impurities in the fuels, even at concentrations as high as 5-10 vol.% [12-14]. Recently, composite electrodes based on substituted $SrVO_{3-\delta}$ were also tested as anodes for protonic SOFC and fuel electrodes of solid oxide electrolysis cell [21-23].

The main drawback of $SrVO_{3-\delta}$ as an SOFC fuel electrode material is the limited stability of the perovskite lattice, which is restricted to reducing conditions. At 1073 K, the high-$p(O_2)$ stability boundary was reported to correspond to ~ 10^{-17} atm [6], while, on heating in air, V^{4+}-based $SrVO_{3-\delta}$ is easily oxidized to V^{5+}-based strontium pyrovanadate $Sr_2V_2O_7$. This redox-induced transformation is accompanied with excessive dimensional changes [15,18] and is not fully reversible at temperatures below 1273 K, at least in a reasonable time span [18].

The present work aims at the development of $SrVO_{3-\delta}$ derivatives with improved redox stability, while retaining sufficient electrical conductivity. Appropriate substitutions may be selected considering the Goldschmidt tolerance factor, a well-known criterion reflecting the formability and stability of perovskite lattice [24] that should be close to unity for ideal cubic perovskite structure. Partial substitution of vanadium with higher-valence transition metal cations,

such as Nb^{5+}, Ta^{5+}, W^{6+} or Mo^{6+}, should shift the tolerance factor closer to the ideal condition by increasing the average cationic radii of B-site species, because higher-valence cations contribute to partial reduction of V^{4+} to larger V^{3+}, and also because the ionic radii of Nb^{5+}, Ta^{5+}, W^{6+} or Mo^{6+} exceed the radius of V^{4+}. Secondly, partial substitution of vanadium with higher-valence cations may oppose its oxidation to pentavalent state. The electronic conductivity of $SrVO_{3-\delta}$-based materials is also likely to change with additions of aliovalent species due to their impact on distribution of valence states of vanadium cations [17,25,26].

This study focused on the effects of substitution with niobium cations in the vanadium sublattice on the stability and properties of perovskite-type strontium vanadate. The emphasis is on the properties relevant for fuel electrode applications, including electrical conductivity and thermochemical expansion under operation conditions, and redox behavior on eventual exposition to oxidizing or inert atmospheres.

2. Experimental

The powders of $SrV_{1-x}Nb_xO_{3-\delta}$ (x = 0, 0.03, 0.05, 0.10, 0.20 and 0.30) were prepared by solid state reaction starting from $SrCO_3$ (≥ 99.9%, Sigma Aldrich), V_2O_5 (≥ 99%, Fluka) and Nb_2O_5 (> 99.9%, Alfa Aesar). Prior to weighing, niobium oxide was calcined in air at 873 K for 2 h to remove adsorbates. Weighed and mixed components were pre-reacted in air at 773 K and 873 K, for 5 h at each temperature, with intermediate regrinding. Then, the pelletized powders were calcined at 1173 K (3×5 h with intermediate regrinding) in flowing 10%H_2-N_2 atmosphere, and subsequently subjected to high-energy milling (Retsch PM 100 planetary ball mill, 650 rpm, 3h, nylon containers with Tosoh tetragonal zirconia milling media). After milling, the powders were compacted uniaxially at 40 MPa into disk-shaped samples and sintered in 10%H_2-N_2 atmosphere at 1773 K for 10 h. Sintering was performed using alumina plates as supports with an interlayer of vanadate powder of the same composition to avoid interactions with the alumina substrate.

Sintered ceramic samples were cut into rectangular bars and polished for dilatometric and electrical measurements. The experimental density was calculated from the mass and geometric dimension of the samples. Powdered samples for X-ray diffraction (XRD) and thermal analysis were prepared by grinding sintered ceramics in a mortar.

XRD patterns were recorded at room temperature using PANalytical X'Pert PRO diffractometer (CuK_α radiation). Unit cell parameters were calculated using Fullprof software (profile match method). Microstructural characterization was performed by scanning electron microscopy (SEM, Hitachi SU-70 instrument) coupled with energy dispersive spectroscopy (EDS, Bruker Quantax 400 detector). The dilatometric measurements (vertical Linseis L70/2001 instrument) and thermogravimetric analysis (TGA, Setaram SetSys 16/18 instrument, sensitivity 0.4 μg, initial sample

weight ~ 0.5 g) were carried out in flowing air or 10%H_2-N_2 mixture at 298-1273 K with constant heating/cooling rate 2-3 K/min or isothermally as function of time.

Electrical conductivity was studied as function of temperature and oxygen partial pressure using 4-probe DC technique under reducing conditions imposed by H_2-H_2O-N_2 mixtures. Isothermal conductivity measurements in redox cycles were performed using impedance spectroscopy (Agilent 4284A precision LCR meter) with automated data acquisition.

In all cases (ceramic processing and measurements), oxygen partial pressure in gas mixtures was monitored by electrochemical YSZ oxygen sensors. Representative values of $p(O_2)$ corresponded to ~10^{-19} atm in 10%H_2-N_2 mixture at 1173 K and ~5×10^{-5} atm in argon atmosphere.

3. Results and discussion

3.1. Phase composition, structure and microstructure

Fig.1 shows selected XRD patterns of as-prepared $SrV_{1-x}Nb_xO_{3-\delta}$ ceramics. For $x \geq 0.10$, the first sintering attempts after calcinations at 1173 K yielded ceramics samples containing $Sr_3V_2O_8$ and other phase impurities in addition to the target perovskite phase (Fig.1A). Therefore, an intermediate high-energy milling step was introduced to promote the homogenization of precursor powders and to facilitate the phase formation.

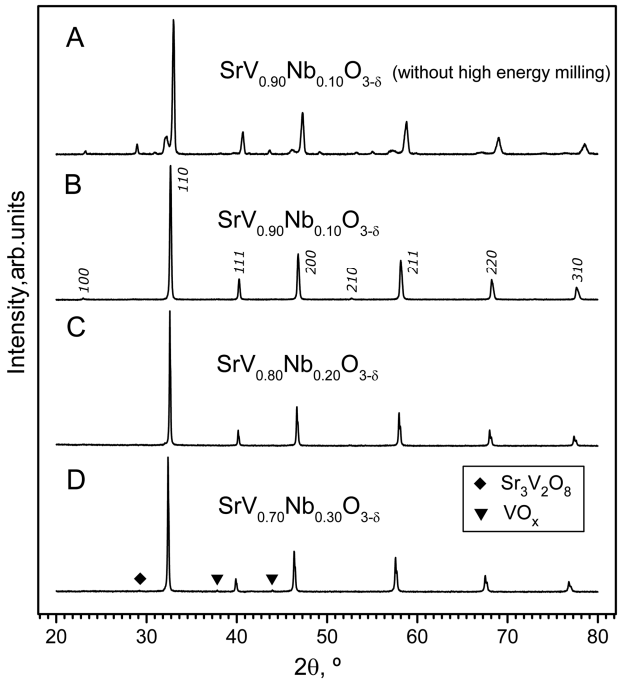

Figure 1. XRD patterns of as-sintered $SrV_{1-x}Nb_xO_{3-\delta}$ ceramics. Marked reflections are indexed according to JCPDS PDF #81-1844 ($Sr_3V_2O_8$) and #75-0048 (VO_x).

As-prepared compositions with $x \leq 0.20$ were single-phase with cubic perovskite structure (space group $Pm\bar{3}m$) characteristic for parent $SrVO_{3-\delta}$ (Fig.1B and C). The presence of minor amounts of $Sr_3V_2O_8$ and $VO_{1+\delta}$ impurities was detected in XRD pattern of $SrV_{0.70}Nb_{0.30}O_{3-\delta}$ (Fig.1D). One may conclude, therefore, that, under applied conditions, the solid solution formation range for $SrV_{1-x}Nb_xO_{3-\delta}$ system is limited to $x \approx 0.25$.

The substitution of higher-valence Nb^{5+} cations into V^{4+} sublattice may be charge-compensated by the formation of V^{3+} cations, possibly combined with decrease in residual fraction of pentavalent V^{5+}, and also decrease in concentration of positively charged oxygen vacancies or the corresponding oxygen sub-stoichiometry, as follows:

$$[Nb_B^{\bullet}] + [B_B^{\bullet}] + 2[V_O^{\bullet\bullet}] = [B_B^{\prime}] \quad (1)$$

where symbol B is used for the parent B-site species (vanadium), i.e., $B_B^{\bullet} \equiv V^{5+}$, $B_B^{\times} \equiv V^{4+}$ and $B_B^{\prime} \equiv V^{3+}$, to avoid confusion with the usual notation of V for vacancies. Larger ionic radii of Nb^{5+} (r^{VI} = 0.64 Å) and V^{3+} (r^{VI} = 0.64 Å) cations compared to V^{4+} (r^{VI} = 0.58 Å) [27] explain a continuous increase of unit cell parameter with x (Table 1). One should note that niobium cations may also undergo partial reduction to 4+ oxidation state under reducing conditions, as emphasized by oxygen nonstoichiometry changes in $Nb_2O_{5-\delta}$ (e.g. [28]), reaching oxygen deficiency δ close to 0.1 (i.e. $[Nb^{4+}]/[Nb] \leq 10\%$) in the latter oxide at 1173 K and $p(O_2) \sim 10^{-19}$ atm. Still, this is not expected to play a prevailing effect on overall charge neutrality in $SrV_{1-x}Nb_xO_{3-\delta}$.

Table 1. Properties of as-prepared $SrV_{1-x}Nb_xO_{3-\delta}$ ceramics

x	Unit cell parameter a, Å	Density, g/cm^3	Relative density, %
0	3.8498(3)	4.33	80
0.03	3.8642(4)	4.05	75
0.05	3.8672(4)	3.96	73
0.10	3.8827(3)	4.04	75
0.20	3.9015(3)	5.03	92
0.30	3.9284(5)	3.21	59

Note: theoretical density was calculated neglecting possible oxygen nonstoichiometry

Figure 2(A-C) illustrate the microstructures of prepared ceramic samples. The substitution with Nb suppresses to some extent grain growth under identical processing/sintering conditions. The SEM/EDS elemental mapping confirmed a minor segregation of V-rich phase for the composition with x = 0.30 (Fig.2D). Sintered $SrV_{1-x}Nb_xO_{3-\delta}$ samples were quite porous; for most compositions, the density was ≤ 80% of theoretical (Table 1). Thus, even with the high-energy

mechanical pre-treatment, vanadate powders show rather poor sinterability under reducing conditions at temperatures ≤ 1773 K (which was the upper limit of the experimental equipment available for this work). One should note, however, that, although relatively high porosity results in underestimated values of electrical conductivity, at the same time it also should promote faster re-equilibration of the ceramic samples with the gas atmosphere on temperature and $p(O_2)$ changes.

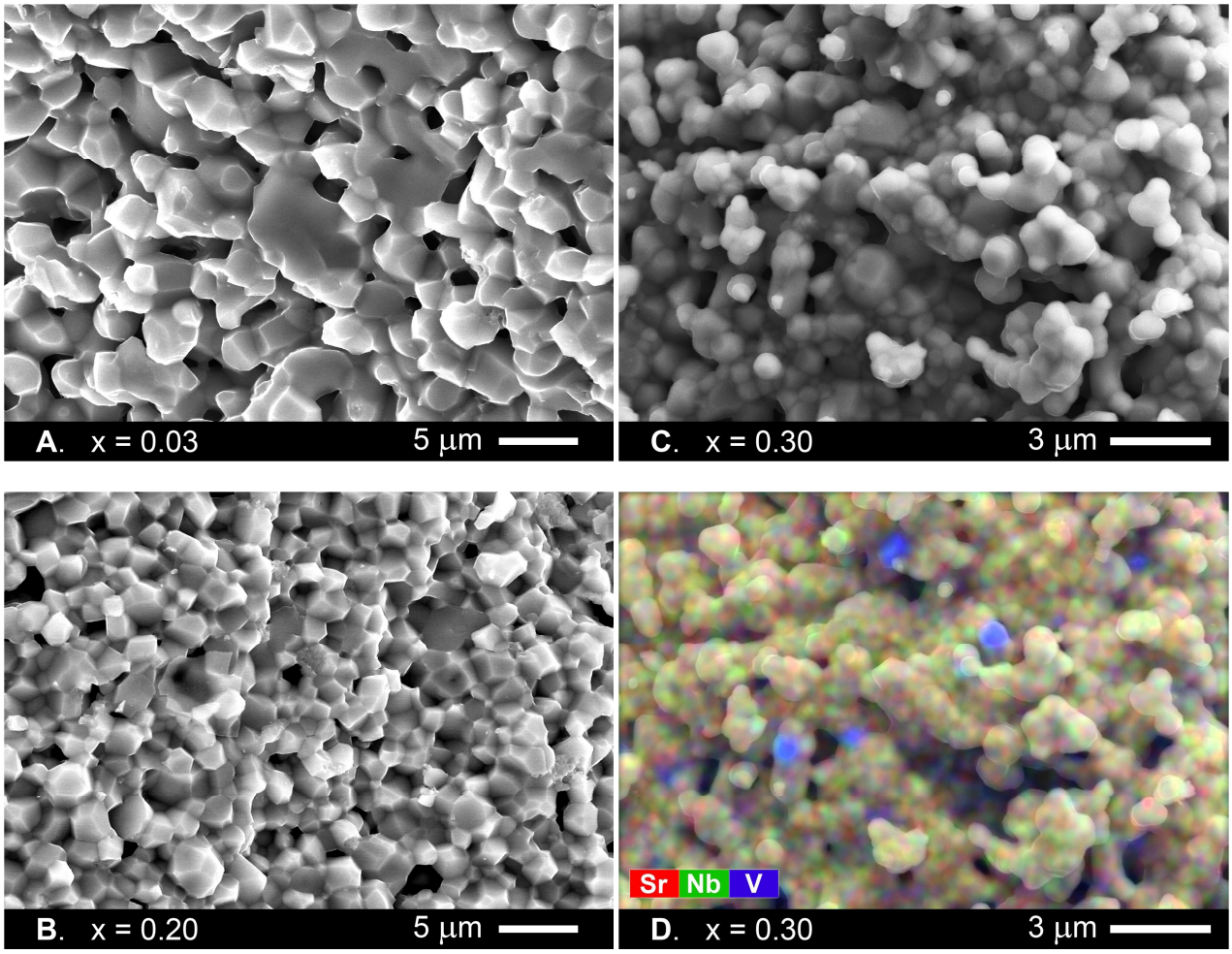

Figure 2. SEM micrographs (A-C) and SEM micrograph with EDS element mapping (D) of fractured cross-sections of as-prepared $SrV_{1-x}Nb_xO_{3-\delta}$ ceramics.

3.2. Thermochemical expansion under reducing conditions

Dilatometric curves of $SrV_{1-x}Nb_xO_{3-\delta}$ ceramics with $x \leq 0.10$ exhibit non-linear behavior under reducing conditions (Fig.3). Similar behavior is characteristic for other $SrVO_3$ derivatives [15] and at least partially can be attributed to a chemical contribution to overall expansion. This phenomenon is well-known for other perovskites with variable-valence transition-metal cations, such as cobaltites and ferrites [29,30], and is associated with redox-induced strain contributions, ascribed to changes in average ionic radii due to gradual changes in average valence state of

transition metal cations combined with conjugate changes in oxygen stoichiometry and effective radius of oxygen vacancies. These redox induced changes depend on oxygen partial pressure and also vary with temperature. Earlier studies confirmed that $SrVO_{3-\delta}$ exhibit non-negligible oxygen deficiency [17-20], although the variation of δ with temperature under reducing conditions at 300-1273 K [18] is much lower compared with, for instance, $(Ba,Sr)Co_{0.8}Fe_{0.2}O_{3-\delta}$ under oxidizing conditions [29].

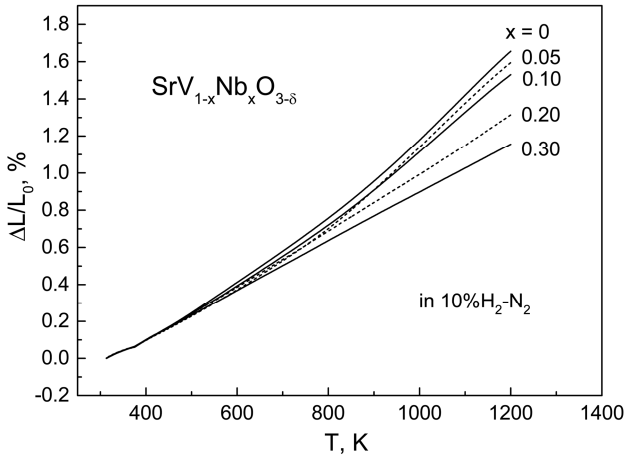

Figure 3. Dilatometric curves of $SrV_{1-x}Nb_xO_{3-\delta}$ ceramics in $10\%H_2$-N_2 atmosphere.

Thermogravimetric studies demonstrated that all $SrV_{1-x}Nb_xO_{3-\delta}$ perovskites lose weight on heating in $10\%H_2$-N_2 atmosphere (Fig.4), corresponding to oxygen release from the lattice. Substitution with higher-valence niobium cations into vanadium sublattice progressively suppresses the weight losses and, therefore, variations of oxygen nonstoichiometry with temperature. In fact, the compositions with x = 0.20 and 0.30 start to lose lattice oxygen only above ~ 800 and 1000 K, respectively, and possibly are oxygen-stoichiometric at lower temperature. The weight change is almost negligible for $SrV_{0.70}Nb_{0.30}O_{3-\delta}$, in correlation with essentially linear behavior of dilatometric curve (Fig.3).

The average thermal expansion coefficients of $SrV_{1-x}Nb_xO_{3-\delta}$ ceramics continuously decrease with increasing Nb content (Table 2). The results indicate that this type of substitution suppresses both true thermal expansion and chemical contribution. The TEC value of $SrV_{0.70}Nb_{0.30}O_{3-\delta}$ approaches that of common solid electrolytes, such as stabilized zirconia or doped ceria and lanthanum gallate, thus ensuring improved thermomechanical compatibility with electrolyte materials.

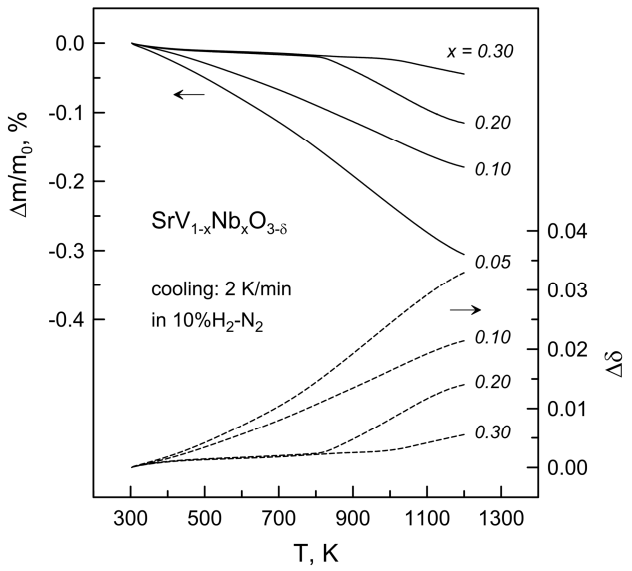

Figure 4. Thermogravimetruc curves of powdered $SrV_{1-x}Nb_xO_{3-\delta}$ ceramics in 10%H_2-N_2 atmosphere, and corresponding relative changes in oxygen deficiency with temperature. Powdered samples were prepared by grinding the sintered pellets.

Table 2. Average thermal expansion coefficients of $SrV_{1-x}Nb_xO_{3-\delta}$ ceramics in 10%H_2-N_2 atmosphere

x	Average TEC	
	Temperature range, K	$(\overline{\alpha}\times10^6) \pm 0.1$, K^{-1}
0	373 – 773 / 773 – 1223	16.1 / 22.7
0.03	373 – 773 / 773 – 1223	14.8 / 23.0
0.05	373 – 773 / 773 – 1223	14.4 / 22.6
0.10	373 – 773 / 773 – 1223	15.2 / 20.5
0.20	373-1223	15.1
0.30	373-1223	13.3

3.3. Electrical conductivity under reducing conditions

Figure 5 shows the electrical conductivity of $SrV_{1-x}Nb_xO_{3-\delta}$ ceramics measured as function of temperature in 10%H_2-N_2 atmosphere. As mentioned above, the experimental values of conductivity should be underestimated due to porosity of the samples; the true values are expected to be ~1.1-2.4 times higher, depending on porosity and pore morphology (e.g. Ref.[31]).

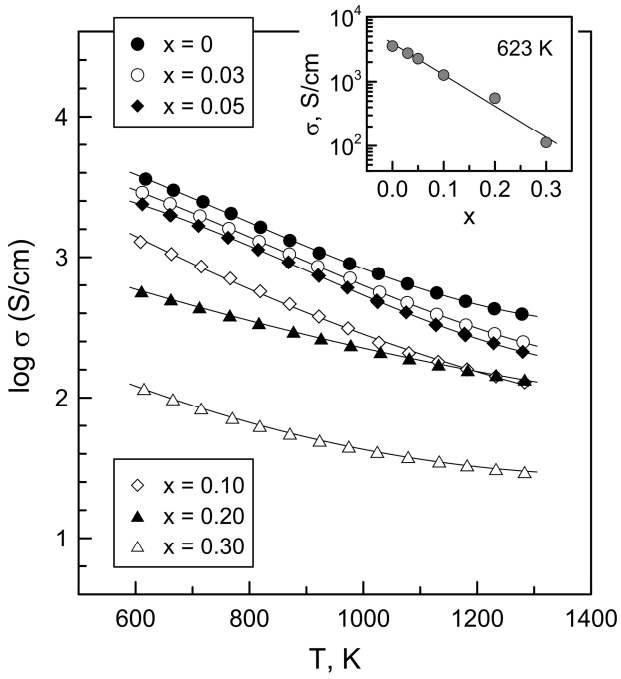

Figure 5. Temperature dependence of electrical conductivity of $SrV_{1-x}Nb_xO_{3-\delta}$ ceramics in 10%H_2-N_2 atmosphere. Inset shows the dependence of electrical conductivity on Nb content at 623 K.

For all studied materials, the electrical conductivity exhibits metallic-like behavior decreasing on heating in the studied temperature range. Substitution with niobium results in a gradual decrease of conductivity. This seems quite reasonable since metallic-type electronic conductivity in $SrVO_3$ perovskite is generally attributed to V^{4+} cations in $3d^1$ configuration forming broad conduction band [17,25,26]. Thus, decrease in electronic conductivity may be ascribed to electron scattering, probably caused by the combined effects of Nb^{5+}, V^{3+}, and possibly even a residual fraction of V^{5+} in B-site positions; this should account for the strong dependence of conductivity on the fraction of Nb (insert in Fig.5). Still, electronic conductivity for most compositions remains above 100 S/cm at 873-1223 K, except for $x = 0.30$.

The dependence of electrical conductivity of $SrV_{1-x}Nb_xO_{3-\delta}$ on $p(O_2)$ is relatively weak under reducing conditions, within the phase stability domain (Fig.6). Such behavior of electronic transport is rather favorable for fuel electrode applications ensuring uniformity of electrical properties across electrode layers under polarization or under variation of fuel gas composition. A slight increase of conductivity with increasing $p(O_2)$ for compositions with $x \leq 0.10$ can be attributed to slight variation of oxygen deficiency in the perovskite lattice and corresponding decrease in the fraction of species responsible for electron scattering (i.e. V^{3+}), as described in subsection 3.4. Dependence of conductivity on $p(O_2)$ is negligible for $SrV_{0.7}Nb_{0.3}O_{3-\delta}$ and $SrV_{0.8}Nb_{0.2}O_{3-\delta}$; this is consistent with the lowest changes in in oxygen deficiency (Fig.4), implying that the concentrations of V^{3+} also remain nearly unchanged in these cases.

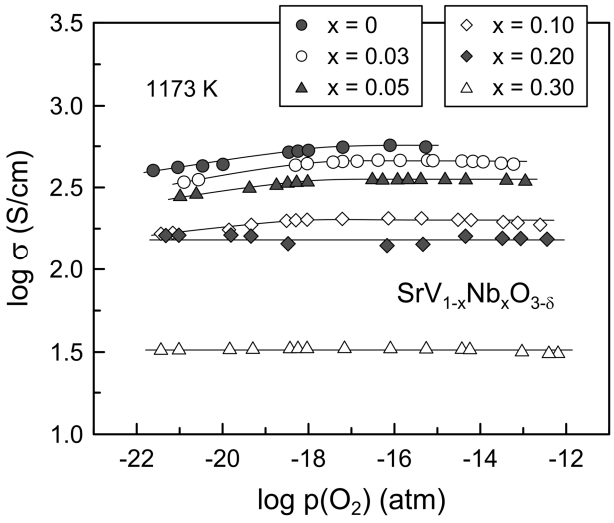

Figure 6. Oxygen partial pressure dependence of electrical conductivity of $SrV_{1-x}Nb_xO_{3-\delta}$ ceramics at 1173 K.

3.4. Defect chemistry guidelines

The impact of Nb-additions in $Sr(V,Nb)O_3$ may be interpreted by expected effects on defect chemistry:

$$SrO + (1-x)BO_2 + 0.5xNb_2O_5 \xrightarrow{-0.25xO_2} Sr_{Sr}^{\times} + (1-2x)B_B^{\times} + xB_B' + xNb_B^{\bullet} + 3O_O^{\times} \qquad (2)$$

This must be combined with changes in oxygen stoichiometry on varying the thermochemical conditions (Fig.4), and corresponding reduction to trivalent V^{3+}, as described by:

$$4B_B^{\times} + 2O_O^{\times} \overset{k_{red}}{\Leftrightarrow} 4B_B' + 2V_O^{\bullet\bullet} + O_2 \qquad (3)$$

Changes in defect chemistry in a generic sample with composition $SrV_{1-x}Nb_xO_{3-\delta}$ may then be described on combining the lattice conservation condition:

$$[B_B^{\times}] + [B_B^{\bullet}] + [B_B'] + [Nb_B^{\bullet}] = 1 \qquad (4)$$

with the mass action constant of the redox reaction (Eq.(3)) and electroneutrality (Eq.(1)); this yields:

$$[B_B^{\times}] = \frac{1+2\delta}{1+2\left(\frac{k_{red}}{p(O_2)}\right)^{1/4}\left(\frac{3-\delta}{\delta}\right)^{1/2}} \qquad (5)$$

$$[B_B'] = \frac{(1+2\delta)\left(\frac{k_{red}}{p(O_2)}\right)^{1/4}\left(\frac{3-\delta}{\delta}\right)^{1/2}}{1+2\left(\frac{k_{red}}{p(O_2)}\right)^{1/4}\left(\frac{3-\delta}{\delta}\right)^{1/2}} \qquad (6)$$

$$[B_B^{\bullet}] = \frac{(1+2\delta)\left(\frac{k_{red}}{p(O_2)}\right)^{1/4}\left(\frac{3-\delta}{\delta}\right)^{1/2}}{1+2\left(\frac{k_{red}}{p(O_2)}\right)^{1/4}\left(\frac{3-\delta}{\delta}\right)^{1/2}} - x - 2\delta \quad (7)$$

In addition, one should take into account possible disproportionation of B-site species, as follows:

$$2B_B^{\times} \overset{k_d}{\Leftrightarrow} B_B^{\bullet} + B_B^{\prime} \quad (8)$$

On combining the corresponding mass action constant $k_d = [B_B^{\bullet}][B_B^{\prime}]/[B_B^{\times}]^2$ with Eqs.(5-7) one obtains:

$$(1-2x-2\delta)\left\{\left(\frac{k_{red}}{p(O_2)}\right)^{1/2}\frac{3-\delta}{\delta}\right\} - (x+2\delta)\left\{\left(\frac{k_{red}}{p(O_2)}\right)^{1/2}\frac{3-\delta}{\delta}\right\}^{1/2} - k_d(1+2\delta) = 0 \quad (9)$$

Eq.(9) reduces to a classic quadratic equation ($ay^2 + by + c = 0$), with $y = \left\{\left[(k_{red}/p(O_2))^{1/2}(3-\delta)/\delta\right]\right\}^{1/2}$, which allows easy defect chemistry simulations for the effects of composition and changes in redox conditions, even if one does not have information on the mass action constant of the oxidation reaction. Still, there is great uncertainty about the disproportionation reaction and the corresponding level of oxidation to pentavalent V^{5+}. In fact, oxidizing conditions give rise to secondary phases with prevailing pentavalent V^{5+}, namely $Sr_2V_2O_7$ or $Sr_3V_2O_8$ [18], suggesting that stability of the perovskite structure is critically affected by oxidation to pentavalent vanadium, and that the energetics of incorporation of V^{5+} in the perovskite lattice is unfavorable. Thus, one may consider a plausible condition when the mass action constant of reaction (8) is very low (k_d << 1), allowing one to neglect the contribution of $[B_B^{\bullet}]$ to charge neutrality, which corresponds to values of k_d in the order of 10^{-3} or lower, as illustrated in Fig.7. Otherwise, the concentrations of V^{3+} and V^{5+} and their contribution to electron scattering should increase with the mass action constant of disproportionation. The limiting condition for negligible fraction of pentavalent vanadium ions is readily obtained for a simplified neutrality condition $[Nb_B^{\bullet}] \approx [B_B^{\prime}] - [B_B^{\bullet}] - 2[V_O^{\bullet\bullet}]$, which can be combined with Eqs.(4-5) to yield:

$$k_{red} = p(O_2)\left(\frac{\delta}{3-\delta}\right)^2\left(\frac{x+2\delta}{1-2x-2\delta}\right)^4 \quad (10)$$

The impact of additions of Nb^{5+} is simulated in Fig.8, with significant increase in trivalent V^{3+}, decrease in oxygen stoichiometry and mainly suppression of pentavalent V^{5+}. Note that the corresponding changes in tetravalent V^{4+} are relatively small, thus confirming that decrease in conductivity by at least one order of magnitude (Fig.5) should be ascribed to electron scattering rather than decrease in concentration of carriers. The combined effects of Nb additions on concentrations of trivalent V^{3+} and pentavalent V^{5+} (Fig.8) also indicate that this species does not affect significantly the electronic conductivity.

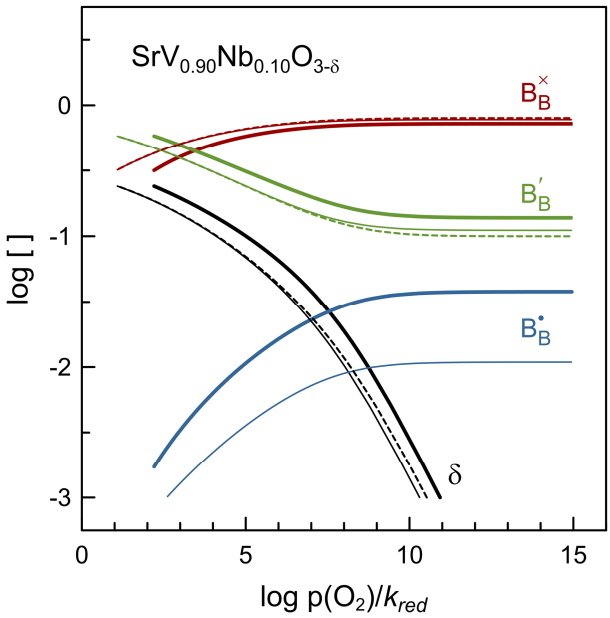

Figure 7. Simulated Kroger-Vink diagrams for $SrV_{0.90}Nb_{0.10}O_{3-\delta}$ computed for different values of the mass action constant of disproportionation reaction k_d =10^{-2} (thick lines) and 2×10^{-3} (thin lines). The limiting solutions for negligible disproportionation (and negligible concentration of pentavalent V^{5+}) are shown dashed.

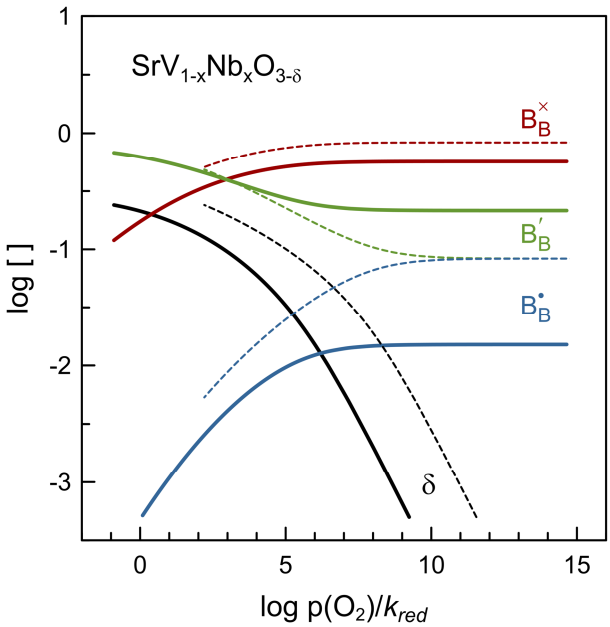

Figure 8. Simulated Kroger-Vink diagrams for $SrV_{0.80}Nb_{0.20}O_{3-\delta}$ (solid lines) and $SrVO_{3-\delta}$ (dashed lines) computed on assuming k_d = 10^{-2}.

3.5. Stability boundary of cubic perovskite phase

The upper $p(O_2)$-stability boundaries of the cubic perovskite phase of $SrV_{1-x}Nb_xO_{3-\delta}$ at 1173 K were determined from the sudden break of *log* σ - *log* $p(O_2)$ dependencies as illustrated in Fig.9A. Electrical conductivity was measured on step-wise increase of oxygen partial pressure and equilibration at each $p(O_2)$ until abrupt drops in conductivity values were observed. These drops were attributed to the onset of decomposition of cubic perovskite phase and segregation of strontium orthovanadate $Sr_3V_2O_8$ which has conductivity 6-7 orders of magnitude lower compared to $SrVO_{3-\delta}$ at 1173 K [18]. The presence of $Sr_3V_2O_8$ phase was confirmed by post-mortem XRD analysis (Fig.10). Thus, the $p(O_2)$ value between the last two data points was considered as an approximate phase stability limit for a given composition.

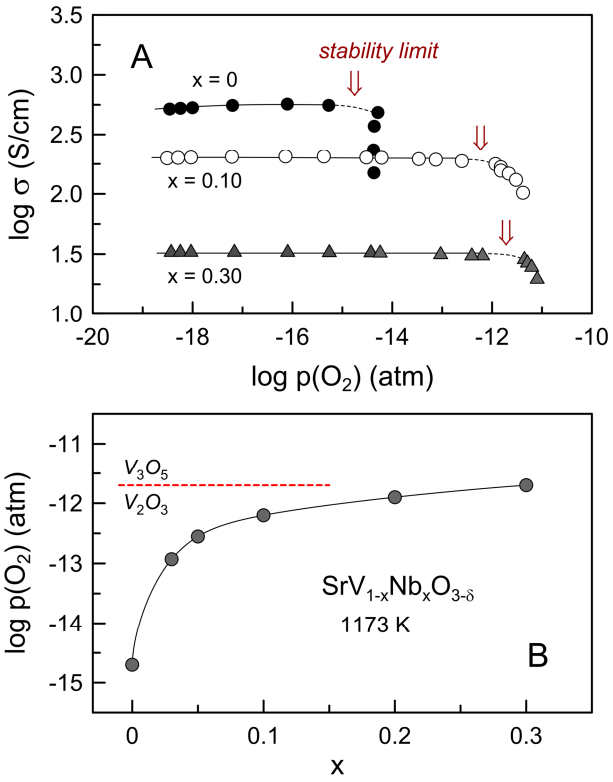

Figure 9. (A) Determination of approximate stability limits of $SrV_{1-x}Nb_xO_{3-\delta}$ perovskites from *log* σ - *log* $p(O_2)$ dependencies, and (B) approximate high-$p(O_2)$ stability boundary of perovskite phase for $Sr(V,Nb)O_{3-\delta}$ system at 1173 K. Dotted horizontal line in (B) marks the phase boundary between V_2O_3 and V_3O_5 at this temperature [32].

Substitution with Nb results in gradual increase of perovskite lattice stability, shifting the upper $p(O_2)$ phase boundary from ~ 2×10^{-15} atm for $SrVO_{3-\delta}$ to ~ 2×10^{-12} atm for $SrV_{0.70}Nb_{0.30}O_{3-\delta}$ (Fig.9B). Note that all studied $SrV_{1-x}Nb_xO_{3-\delta}$ perovskites exhibit better redox stability compared to undoped vanadium oxides: at 1173 K, the high-$p(O_2)$ stability boundary of V_2O_3 and low-$p(O_2)$ stability boundary of VO_2 correspond to 2×10^{-12} atm and 7×10^{-9} atm, respectively, with mixed 3+/4+ valence vanadium oxides existing in the intermediate range (e.g. Refs.[32,33]). Still, the

decomposition of even $SrV_{0.70}Nb_{0.30}O_{3-\delta}$ occurs at much lower oxygen partial pressure than that desired for practical application.

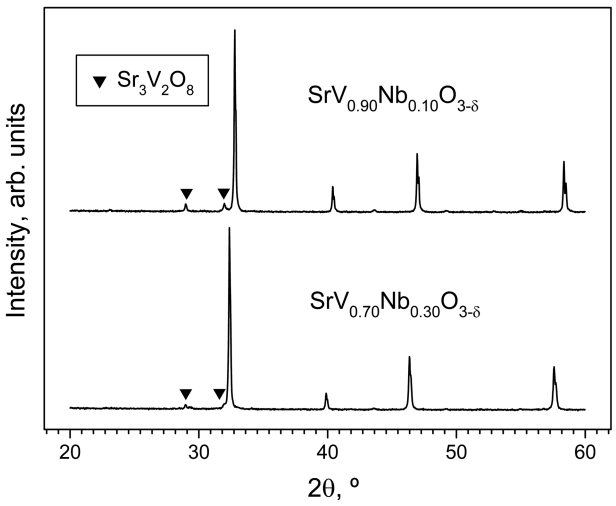

Figure 10. XRD patterns of $SrV_{1-x}Nb_xO_{3-\delta}$ ceramics after phase stability boundary determination (see Fig.9A). Marked reflections are indexed according to JCPDS PDF # 81-1844.

The effects of Nb on stability may be understood if one considers the point defect model to predict changes in tolerance factor, based on Shannon ionic radii [27], with the average ionic radius of B-site species, i.e.:

$$\tau = \frac{r_{O^{2-}} + r_{Sr^{2+}}}{\sqrt{2}\left(r_{O^{2-}} + [B_B^{\times}]r_{V^{4+}} + [B_B^{\bullet}]r_{V^{5+}} + [B_B^{\prime}]r_{V^{3+}} + [Nb_B^{\bullet}]r_{Nb^{5+}}\right)} \qquad (11)$$

Thus, representative simulations could be computed to examine the evolution from reducing to oxidizing conditions, as demonstrated in Fig.11 for $SrV_{1-x}Nb_xO_{3-\delta}$. These simulations suggest that $SrVO_{3-\delta}$ evolves from a favorable tolerance factor ($\tau \approx 1$) under reducing conditions to less favorable structural and defect chemistry changes under oxidizing conditions ($\tau > 1$). The predicted increase in tolerance factor and corresponding limited redox stability of $SrVO_{3-\delta}$ may be ascribed to onset of a fraction of V^{5+}, by disproportionation (Eq.8). In addition, V^{5+} tends to accept preferential tetrahedral coordination, because the radii ratio $r_{V^{5+}} : r_{O^{2-}} \approx 0.254$ is close to the ideal value ($r_C : r_A \approx 0.225$) expected for 4-fold coordination. Indeed, pentavalent V^{5+} usually assumes tetrahedral coordination in oxide compounds, as found for the orthovanadate phase $Sr_3V_2O_8$ (space group $R\bar{3}m$) [34]; this is the preferential reaction product observed after oxidative decomposition of $SrV_{1-x}Nb_xO_{3-\delta}$ oxides, as confirmed by XRD. Additions of Nb lower the tolerance factor, by increasing the concentrations of larger B-site cations (i.e. Nb^{5+} and V^{3+}), suppressing onset of pentavalent V^{5+} and also approaching the ideal value ($\tau \approx 1$) under oxidizing.

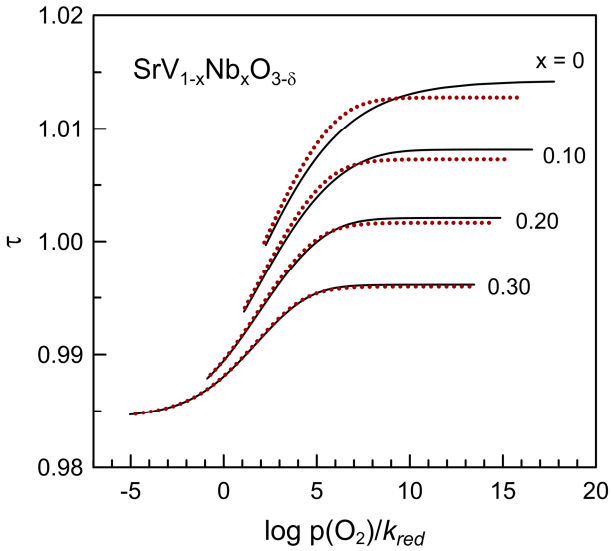

Figure 11. Predictions of tolerance factor of $SrV_{1-x}Nb_xO_{3-\delta}$ and its dependence on redox changes based on defect concentrations (Eq.(11)). Solid lines were computed on assuming negligible disproportionation ($k_d \approx 0$), and dotted lines were computed for $k_d \approx 0.04$.

3.6. Oxidative decomposition vs metastable redox stability under inert atmosphere

Figure 12 shows the relaxation of electrical conductivity of $SrV_{0.80}Nb_{0.20}O_{3-\delta}$ ceramics upon reducing → oxidizing → reducing and reducing → inert → reducing cycling at 1173 K. After changing the atmosphere from reducing to oxidizing, the conductivity dropped rapidly by more than 4 orders of magnitude in a few hours and then slowly continued to decrease. Obviously, this is associated with onset of insulating phases, such as $Sr_2V_2O_7$ and $Sr_3V_2O_8$, as revealed by X-ray diffraction. Switching back to reducing atmosphere resulted in a reverse reduction of the sample and fast restoration of conductivity level. In fact, electrical conductivity at the end of redox cycling was even approximately 10% higher compared to initial value. Post-mortem XRD analysis showed the presence of two secondary phases - $Sr_3V_2O_8$ and a Nb-lean secondary perovskite - in addition to main perovskite phase (Fig.13A). XRD peaks of this secondary perovskite are clearly displaced to higher angles, showing that its unit cell parameter is closer to that of undoped $SrVO_{3-\delta}$, which possesses superior electrical conductivity. Thus, the enhanced conductivity of the secondary perovskite explains the unexpected final gain in conductivity after partial oxidative decomposition. Cross-section SEM inspections demonstrated the presence of cracks (Fig.14A) and significant microstructural changes close to the surface (Figs.14B and C, as compared to Fig.2B), whereas the microstructure in middle of sample remained mostly unchanged. Furthermore, SEM/EDS analysis of near-surface areas confirmed phase separation, with Nb-enriched and Nb-depleted grains (Fig.14D).

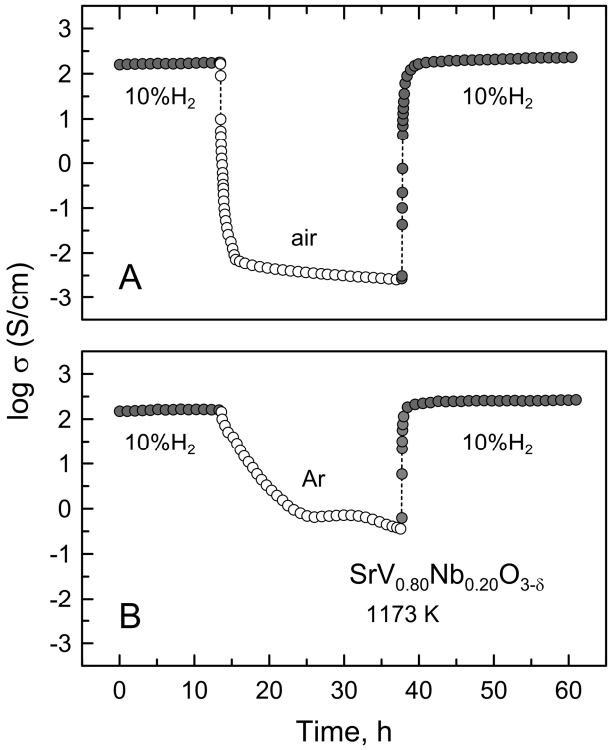

Figure 12. Relaxation of electrical conductivity of $SrV_{0.80}Nb_{0.20}O_{3-\delta}$ ceramics in (A) $10\%H_2 \rightarrow air \rightarrow 10\%H_2$ and (B) $10\%H_2 \rightarrow air \rightarrow 10\%H_2$ redox cycles at 1173 K.

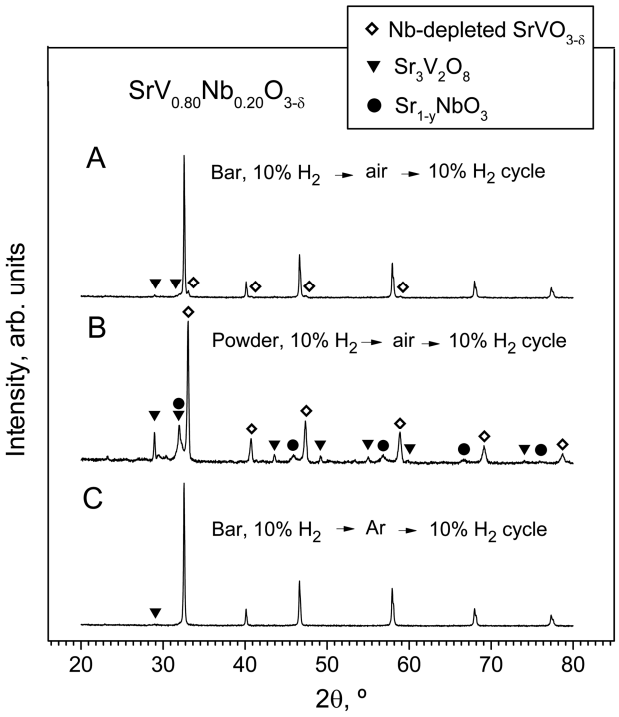

Figure 13. XRD patterns of $SrV_{0.80}Nb_{0.20}O_{3-\delta}$ samples after redox cycling at 1173 K. Patterns (A) and (C) were obtained after conductivity relaxation studies, performed with bulk ceramic samples (Fig.12), and pattern (B) was obtained after thermogravimetric studies of crushed samples (see Fig.15). Marked reflections are indexed according to JCPDS PDF # 81-0119 ($SrVO_{3-\delta}$), # 81-1844 ($Sr_3V_2O_8$) and # 80-2497 ($Sr_{0.72}NbO_3$).

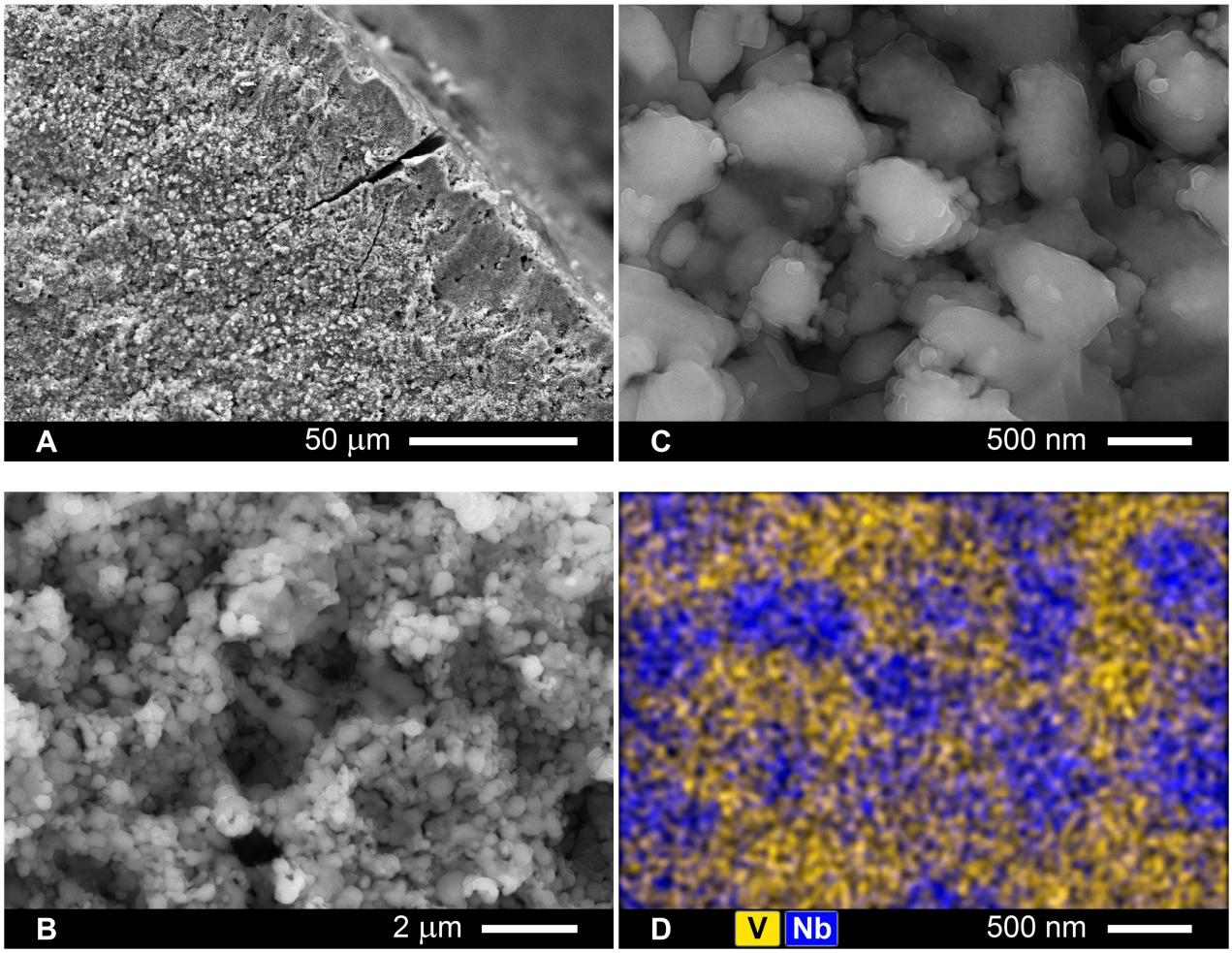

Figure 14. (A-C) SEM micrographs of fractured cross-section of $SrV_{0.80}Nb_{0.20}O_{3-\delta}$ ceramic samples after conductivity relaxation measurements in 10%H_2→air→10%H_2 redox cycle at 1173 K, and (D) EDS elemental mapping corresponding to micrograph (C).

Thermogravimetry of powdered ceramic samples shows even faster oxidative decomposition in air (Fig.15), as expected by magnifying the area for oxygen exchange. Post-mortem X-ray diffraction (Fig.13B) showed co-segregations of $Sr_3V_2O_8$ and $Sr_{1-x}NbO_3$, whereas reflections of the major perovskite phase are shifted to slightly higher angles; this shrinkage of the unit cells corresponds to residual Nb-lean compositions $SrV_{0.8+y}Nb_{0.2-y}O_{3-\delta}$, as shown in Fig.16. Note also that structural characterization provides clear guidelines for the overall conservation of Sr, V and Nb in the residual perovskite and secondary phases.

Real-time electrical conductivity relaxation of $SrV_{0.80}Nb_{0.20}O_{3-\delta}$ during the reducing → inert → reducing cycle shows slower evolution from 10%H_2-N_2 to argon atmosphere (Fig.12), partly due to slower stabilization of oxygen partial pressure in the gas phase. The conductivity decreased with nearly constant rate in first 10 h, after changing from reducing

to inert atmosphere, followed by much slower degradation after stabilization of $p(O_2)$ in gas flow. Note also that the overall drop of conductivity after 24 h of oxidation in Ar was ~ 2 orders of magnitude less compared to oxidation in air. Inverse reduction results in rapid recovery and even slight increase of conductivity level, as reported previously for changes induced by the reducing → oxidizing → reducing cycle. However, post-mortem SEM analysis after reducing → inert → reducing cycling did not reveal any noticeable microstructural changes, and only negligible traces of $Sr_3V_2O_8$ phase were detected in corresponding XRD pattern (Fig.13C). These results demonstrate that oxidative decomposition of $SrV(Nb)O_{3-\delta}$ is kinetically limited under inert atmosphere, thus making possible the fabrication of $SrVO_3$-based electrodes in these conditions. Prospects for metastable tolerance to inert atmospheres are even more obvious after relatively long-term (20 h) exposition to inert atmosphere at 1173 K (Fig.17). Only minor traces of $Sr_3V_2O_8$ phase can be detected in XRD patterns, almost at background level. In addition, changes in lattice parameter are relatively small and indicate that the composition of the perovskite phase remains nearly unchanged (Fig.16).

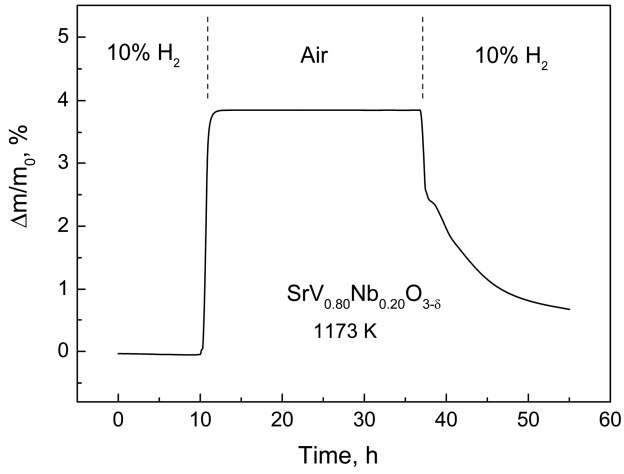

Figure 15. Relative weight change of powdered $SrV_{0.80}Nb_{0.20}O_{3-\delta}$ sample in $10\%H_2 \rightarrow air \rightarrow 10\%H_2$ redox cycle at 1173 K.

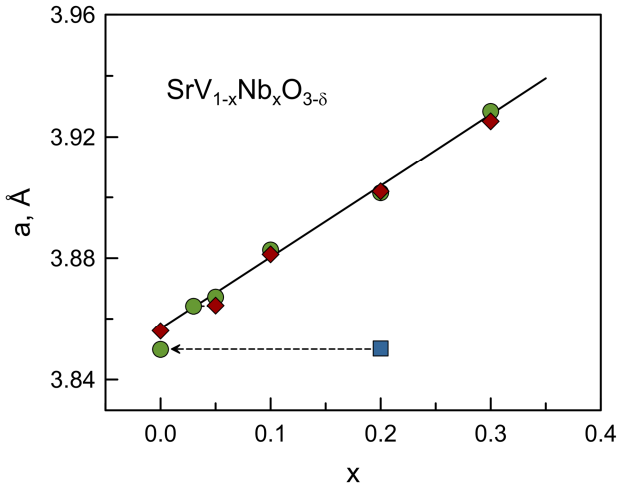

Figure 16. Lattice parameter values obtained for the as-prepared $SrV_{1-x}Nb_xO_{3-\delta}$ samples (circles) and for the corresponding residual Nb-lean perovskites $SrV_{1-x+y}Nb_{x-y}O_{3-\delta}$ after exposing powdered samples to the reducing → inert → reducing cycle (diamonds) or reducing → oxidizing → reducing cycle (square). Dotted lines show the expected changes in composition.

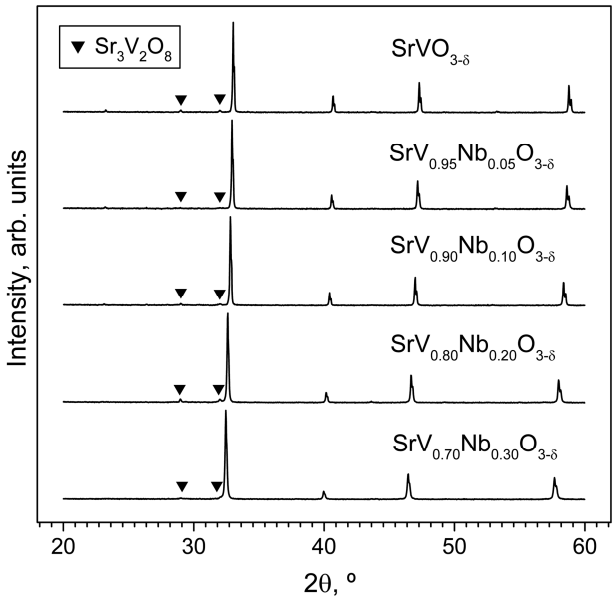

Figure 17. XRD patterns of powdered $SrV_{1-x}Nb_xO_{3-\delta}$ ceramic samples after thermal treatment in Ar flow at 1173 K for 20 h. Marked reflections are indexed according to JCPDS PDF #81-1844.

4. Conclusions

(i) $SrV_{1-x}Nb_xO_{3-\delta}$ (x = 0-0.30) ceramics were prepared by solid-state synthesis under reducing conditions and sintered at 1773 K in 10%H_2-N_2 flow. XRD and SEM/EDS studies showed that the single-phase cubic perovskite range is up to $x \approx 0.25$;

(ii) $SrV_{1-x}Nb_xO_{3-\delta}$ ceramics exhibit metallic-like electrical conductivity, which is nearly p(O_2)-independent and decreases with niobium substitution; this still exceeds 100 S/cm at temperatures below 1273 K for compositions with $x \leq 0.20$;

(iii) Substitution with niobium extends the stability domain of cubic perovskite phase shifting the high-p(O_2) stability boundary from ~ 2×10^{-15} atm for undoped $SrVO_{3-\delta}$ to ~ 2×10^{-12} atm for x = 0.30;

(iv) Substitution with niobium also suppresses partly the thermochemical expansion characteristic for parent $SrVO_{3-\delta}$, by lowering changes in oxygen deficiency and concentration of partially reduced V^{3+} cations occurring under reducing conditions; this improves the thermomechanical compatibility with solid electrolytes;

(v) Defect chemistry modeling provides useful guidelines to understand the role of Nb additions on redox and oxygen stoichiometry changes, and their impact on properties and stability;

(v) $SrV_{1-x}Nb_xO_{3-\delta}$ perovskites undergo oxidative decomposition in air without complete reversibility, even after relatively short redox cycles at temperatures below 1273 K. Still, decomposition is kinetically stagnated under inert gas conditions suggesting reversible or nearly reversible behavior in short-term redox cycling between reducing and inert atmospheres.

Acknowledgements

This work was developed within the projects SFRH/BD/91675/2012, PTDC/CTM-CER/118933/2010, IF/01072/2013/CP1162/CT0001, and project CICECO-Aveiro Institute of Materials (Ref. FCT UID/CTM/50011/2013), financed by national funds through the FCT/MEC and when applicable co-financed by FEDER under the PT2020 Partnership Agreement.

References

1. Y.H. Heo, J.W. Lee, S.B. Lee, T.H. Lim, S.J. Park, R.H. Song, C.O. Park and D.R. Shin, *Int. J. Hydrogen Energy*, 2011, **36**, 797.
2. D. Sarantaridis and A. Atkinson, *Fuel Cells*, 2007, **7**, 246.
3. X.M. Ge, S.H. Chan, Q.L. Liu and Q. Sun, *Adv. Energy Mater*., 2012, **2**, 1156.
4. Y. Matsuzaki and I. Yasuda, *Solid State Ionics*, 2000, **132**, 261.
5. S. Hui and A. Petric, *Solid State Ionics*, 2001, **143**, 275.
6. Z. Cheng, S. Zha, L. Aguilar and M. Liu, *Solid State Ionics*,2005, **176**, 1921.
7. X.M. Ge and S.H. Chan, *J. Electrochem. Soc*., 2009, **156**, B386.
8. J.S. Park, I.D. Hasson, M.D. Gross, C. Chan, J.M. Vohs and R.J. Gorte, *J. Power Sources*, 2011, **196**, 7488.
9. M. Cooper, K. Channa, R. De Silva and D.J. Bayless, *J. Electrochem. Soc.*, 2010, **157**, B1713.
10. L. Aguilar, S. Zha, Z. Cheng, J. Winnick and M. Liu, *J. Power Sources*, 2004, **135**, 17.
11. K. Tamm, R. Küngas, R.J. Gorte and E. Lust, *Electrochimica Acta*, 2013, **106**, 398.
12. C. Peng, J. Luo, A.R. Sanger and K.T. Chuang, *Chem. Mater*., 2010, **22**, 1032.
13. Z. Cheng, S. Zha, L. Aguilar, D. Wang, J. Winnick and M. Liu, *Electrochem. Solid State Lett.*, 2006, **9**, A31.
14. X. Ge, L. Zhang, Y. Fang, J. Zeng and S.H. Chan, *RSC Advances*, 2011, **1**, 715.
15. A.A. Yaremchenko, B. Brinkmann, R. Janssen and J.R. Frade, *Solid State Ionics*, 2013, **247-248**, 86.
16. T. Maekawa, K. Kurosaki and S. Yamanaka, *J. Alloy. Compd.*, 2006, **426**, 46.
17. P. Dougier, J.C.C. Fan and J.B. Goodenough, *J. Solid State Chem.*, 1975, **14**, 247.
18. J. Macías, A.A. Yaremchenko and J.R. Frade, *J. Alloy. Compd.*, 2014, **601**, 186.
19. M.J. Rey, Ph. Dehaudt, J.C. Joubert, B. Lambert-Andron, M. Cyrot and F. Cyrot-Lackmann, *J. Solid State Chem.*, 1990, **86**, 101.
20. T. Shin-ike, T. Sakai, G. Adachi and J. Shiokawa, *Mater. Res. Bull.*, 1976, **11**, 249.
21. S.-H. Song, S.-E. Yoon, J. Choi, B.-K. Kim and J.-S. Park, *Int. J. Hydrogen Energy*, 2014, **39**, 16534.
22. Y. Li, G. Wu, C. Ruan, Q. Zhou, Y. Wang, W. Doherty, K. Xie and Y. Wu, *J. Power Sources*, 2014, **253**, 349.
23. S.-E. Yoon, S.-H. Song, J. Choi, J.-Y. Ahn, B.-K. Kim and J.-S. Park, *Int. J. Hydrogen Energy*, 2014, **39**, 5497.
24. M.A. Peña and J.L.G. Fierro, *Chem. Rev.*, 2001, **101**, 1981.
25. V. Giannakopoulou, P. Odier, J.M. Bassat and J.P. Loup, *Solid State Commun.*, 1995, **93**, 579.
26. T. Palanisamy, J. Gopalakrishnan and M.V.C. Sastri, *Z. Anorg. Allg. Chem.*, 1975, **415**, 275.
27. R.D. Shannon, *Acta Crystallogr. A*, 1976, **32**, 751.
28. P. Kofstad, *J. Less-Common Met.*, 1968, **14**, 153.

29. A.A. Yaremchenko, S.M. Mikhalev, E.S. Kravchenko and J.R. Frade, *J. Eur. Ceram. Soc.*, 2014, **34**, 703.

30. M. Kuhn, S. Hashimoto, K. Sato, K. Yashiro and J. Mizusaki, *Solid State Ionics*, 2013, **241**, 12.

31. J. Mizusaki, S. Tsuchiya, K. Waragai, H. Tagawa, Y. Arai and Y. Kuwayama, *J. Am. Ceram. Soc.*, 1996, **79**, 109.

32. H. Okinaka, K. Kosuge and S. Kachi, *T. Jpn. I. Met.*, 1971, **12**, 44.

33. L. Brewer and B.B. Ebbinghaus, *Thermochim. Acta*, 1988, **129**, 49.

34. A. Durif, *Acta Crystallogr.*, 1959, **12**, 420.